

Investigation of the Impact of Active Short Circuit on Traction Inverter

Downloaded from: https://research.chalmers.se, 2026-11-22 18:02 UTC

Citation for the original published paper (version of record):
Lai, L., Brzycki, M., Sharma, N. et al (2026). Investigation of the Impact of Active Short Circuit on Traction Inverter. 2026 International Power Electronics Conference IPEC Nagasaki 2026 Ecce Asia. http://dx.doi.org/10.23919/IPEC-Nagasaki2026-EC64663.2026.11597256

N.B. When citing this work, cite the original published paper.

research.chalmers.se offers the possibility of retrieving research publications produced at Chalmers University of Technology. It covers all kind of research output: articles, dissertations, conference papers, reports etc. since 2004. research.chalmers.se is administrated and maintained by Chalmers Library

(article starts on next page)

Investigation of the Impact of Active Short Circuit on Traction Inverter

Linhua Lai[1*], Maciej Brzycki[1], Nimananda Sharma[2], Artem Rodionov[1], Yujing Liu[1*]
1 Department of Electrical Engineering, Chalmers University of Technology, Gothenburg, Sweden
2 Volvo group, Gothenburg, Sweden
*linhua@chalmers.se, yujing.liu@chalmers.se

***Abstract*—When faults occur in the drivetrain of an electric vehicle, the switches of the inverter can be turned on simultaneously to isolate the DC-link from the machine, which is referred to as active short circuit (ASC). However, the surge current during ASC may damage the inverter. This paper investigates the impact of ASC current on the inverter. A model describing the transient current under ASC for permanent magnet synchronous machine (PMSM) is presented. To evaluate the thermal stress, inverter loss and thermal models are introduced. Then, simulations of a PMSM and three-phase inverter system are conducted using PLECS. The worst rotor angle for ASC triggering is identified across the full operating range of the PMSM. Furthermore, different operating points are analyzed to determine the highest thermal stress due to ASC. Results show that the most critical condition occurs when the machine operates with base speed and rated torque.**

***Keywords*—Active short circuit, Reliability, Silicon carbide (SiC) inverter, Traction motors.**

I. Introduction

Permanent magnet synchronous machines (PMSMs) are widely used in the drivetrain system of automotives due to their high efficiency and power density[1]. These machines are typically driven by inverters that convert DC power from the battery into AC power for the operation of motor. Once a fatal fault is detected in the drivetrain such as a loss of connection to vital sensors or a breakdown of battery isolation, actions should be taken in the inverter to bring the vehicle torque to a controllable value.

Active short circuit (ASC) is a fault-handling strategy that can safely transition the system into a controllable state. In ASC mode, either the top switches or the bottom switches are turned on simultaneously[2], and therefore the motor terminals are short-circuited. The electric motive force (EMF) produced by the rotor is applied on the winding impedances. Since the motor remains three-phase balanced, the DC-link is electrically isolated, eliminating the risk of over-voltage[3], [4]. However, the surge current during the transient of ASC is higher than the normal operating current of the drivetrain, which may induce additional stress on the power transistors in the inverter. To ensure reliable inverter operation, the inverter should have enough capability to withstand the highest surge current during the ASC mode[5].

Previous studies have developed analytical models for both transient and steady-state ASC currents in PMSMs, showing that the peak surge current depends on the initial dq-currents, rotor position, and machine speed[6], [7], [8]. Researches have also examined the impact of short-circuit current on the rest of life of the SiC MOSFET, revealing degradation and failure mechanisms of SiC MOSFET[9], [10], [11]. In summary, prior work has primarily focused on machine-side current behavior or device-level failure mechanisms, while the stress caused by ASC on the inverter remains unclear.

To ensure long-term inverter reliability, it is essential to identify the worst-case ASC condition across the full operating range of a traction motor. The transient thermal stress should be evaluated properly, so the inverter can be sized with enough thermal safety margins. Addressing these issues requires a comprehensive model that captures the inverter's response to ASC and assesses its thermal safety margins.

To fill this research gap, this study investigates the impact of ASC on traction inverters. A transient current model for PMSM under ASC is developed, followed by inverter loss and thermal modeling to quantify the resulting stress. Simulations of a PMSM–inverter system are conducted in PLECS to identify the worst rotor angle for ASC triggering, and the thermal stress is evaluated across various operating points of the machine.

II. Modeling of System Under ASC

A. Modeling of ASC Current

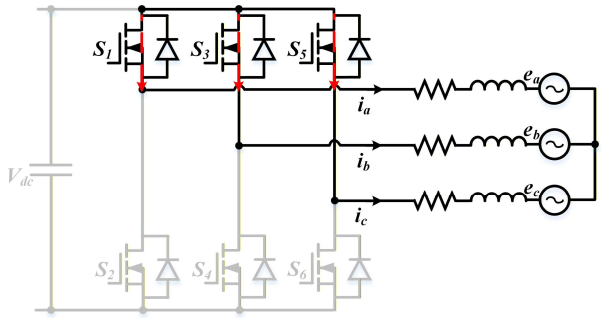


Fig. 1 Equivalent circuit of ASC mode with only the high-side transistors conducting.

When ASC is activated, either the high-side or low-side transistors of the inverter are turned on simultaneously, while the transistors on the opposite side remain off. Fig. 1 illustrates the scenario when the transistors on the high side S_1, S_3, and S_5 are conducting.

Assuming the mechanical time constant of the machine is much higher than the electrical constant, the rotor speed can be considered constant during the transient of ASC. Let t=0 denote the moment when the ASC is trigged. The voltage equations of the PMSM in the dq-reference frame are given by

$$\begin{cases} 0 = L_d \dfrac{di_d}{dt} - \omega L_q i_q + R_s i_d \\ 0 = L_q \dfrac{di_q}{dt} + \omega L_d i_d + R_s i_q + \omega \psi_m \end{cases}, \tag{1}$$

where i_d and i_q are the stator current, L_d and L_q are the incremental stator inductances, R_s is the stator resistance, ω is the electrical angular speed, and ψ_m is the rotor flux linkage. Assuming the machine operates in steady state with constant dq-axis currents before the activation of ASC, initial conditions at t=0 can be obtained as

$$\begin{cases} v_{d(0)} = -\omega L_q i_{q(0)} + R_s i_{d(0)} \\ v_{q(0)} = \omega L_d i_{d(0)} + R_s i_{q(0)} + \omega \psi_m \end{cases} \tag{2}$$

where the initial stator voltages $v_{d(0)}$ and $v_{q(0)}$, and the initial stator current $i_{d(0)}$ and $i_{q(0)}$ are determined by the required output torque and speed of the machine.

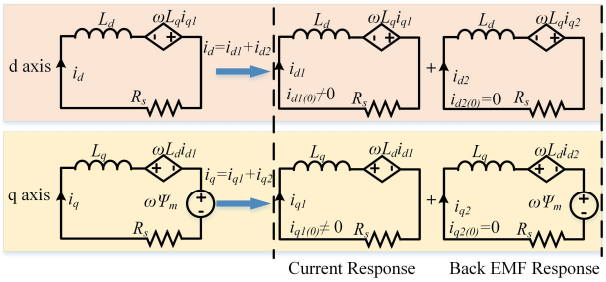


Fig. 2 Equivalent dq-axis circuits of ASC operation

After the ASC is initiated, the current response can be decomposed into two components, as shown in Fig. 2. Denote i_{d1} and i_{q1} as the stator current due to the initial stator current. i_{d2} and i_{q2} are the stator current induced by the machine's EMF. Thus, the total dq-axis currents satisfy:

$$\begin{cases} i_d = i_{d1} + i_{d2} \\ i_q = i_{q1} + i_{q2} \end{cases} \tag{3}$$

with initial conditions

$$\begin{cases} i_{d(0)} = i_{d1(0)}, i_{d2(0)} = 0 \\ i_{q(0)} = i_{q1(0)}, i_{q2(0)} = 0 \end{cases}. \tag{4}$$

Solving (1)-(4), the stator current due to initial conditions is

$$\begin{cases} i_{d1} = \dfrac{i_{d(0)}}{\cos\theta_1} e^{-\frac{t}{\tau}} \cos(\omega t + \theta_1) \\ i_{q1} = \dfrac{i_{q(0)}}{\cos\theta_2} e^{-\frac{t}{\tau}} \cos(\omega t + \theta_2) \end{cases} \tag{5}$$

where the time constant τ, and angles θ_1, θ_2 are defined as

$$\begin{cases} \tan\theta_1 = -\dfrac{1}{\omega\tau} + \dfrac{u_{d(0)}}{\omega L_d i_{d(0)}} \\ \tan\theta_2 = -\dfrac{1}{\omega\tau} + \dfrac{\psi_m}{L_q i_{q(0)}} + \dfrac{R_s}{\omega L_q} + \dfrac{L_d i_{d(0)}}{L_q i_{q(0)}} \end{cases}, \tau = \frac{2L_d L_q}{R_s(L_d + L_q)}. \tag{6}$$

Similarly, the response due to machine EMF is:

$$\begin{cases} i_{d2} = \dfrac{\omega^2 \psi_m L_q}{(\omega^2 L_d L_q + R_s^2)} \left(\dfrac{e^{-\frac{t}{\tau}}}{\cos\theta_3} \cos(\omega t + \theta_3) - 1 \right) \\ i_{q2} = \dfrac{\omega \psi_m R_s}{(\omega^2 L_d L_q + R_s^2)} \left(\dfrac{e^{-\frac{t}{\tau}}}{\cos\theta_4} \cos(\omega t + \theta_4) - 1 \right) \end{cases} \tag{7}$$

with angles θ_3, θ_4 given by

$$\begin{cases} \tan\theta_3 = -\dfrac{1}{\omega\tau} \\ \tan\theta_4 = \dfrac{\omega^2 L_d L_q + R_s^2}{\omega R_s L_q} - \dfrac{1}{\omega\tau} \end{cases}. \tag{8}$$

Then, the full stator currents are derived as

$$\begin{cases} i_d = \dfrac{i_{d(0)}}{\cos\theta_1} e^{-\frac{t}{\tau}} \cos(\omega t + \theta_1) + \dfrac{\omega^2 \psi_m L_q}{(\omega^2 L_d L_q + R_s^2)} \left(\dfrac{e^{-\frac{t}{\tau}}}{\cos\theta_3} \cos(\omega t + \theta_3) - 1 \right) \\ i_q = \dfrac{i_{q(0)}}{\cos\theta_2} e^{-\frac{t}{\tau}} \cos(\omega t + \theta_2) + \dfrac{\omega \psi_m R_s}{(\omega^2 L_d L_q + R_s^2)} \left(\dfrac{e^{-\frac{t}{\tau}}}{\cos\theta_4} \cos(\omega t + \theta_4) - 1 \right) \end{cases}. \tag{9}$$

From equation (9), it is evident that the transient dq-axis currents are independent of the rotor position at the moment ASC is triggered. However, the influence of initial rotor angle, which is denoted as θ_0, on the phase current i_a can be found after applying the inverse d-q transformation:

$$i_a = i_d \cos(\omega t + \theta_0) - i_q \sin(\omega t + \theta_0). \tag{10}$$

To determine the worst rotor position that results in the highest phase current, let the partial derivative $\partial i_a / \partial \theta_0$=0:

$$\frac{\partial i_a}{\partial \theta_0} = 0 \Rightarrow \theta_0 = atan\left(-\frac{i_q(t)}{i_d(t)} \frac{\cos(\omega t + \theta_2)}{\cos(\omega t + \theta_1)} \frac{\cos\theta_1}{\cos\theta_2} \right) - \omega t. \tag{11}$$

Equation (11) shows that the worst rotor position depends on the dq-axis currents, which related to the torque and speed of the machine

B. Losses in Power Transistor

The surge current during ASC generates additional losses in the transistors, resulting in increased junction temperatures. To evaluate the temperature rise during ASC events, both the initial temperature before ASC and the transient temperature during ASC should be calculated. Hence, both the losses incurred during normal operation and those introduced by ASC must be considered.

During the normal operation of the synchronous machine, the inverter is controlled using Space Vector Pulse Modulation (SVPWM). Assuming the conduction time of the body diode is negligible, the average conduction losses in the MOSFETs can be approximated by:

$$P_{c,T} = \frac{R_{on}}{2\pi} \left(\int_0^{2\pi} D(\omega t) I_{rms}^2 \sin^2(\omega t) d(\omega t) \right) \tag{12}$$

where R_{on} is the turn-on resistance of the MOSFET, D is the duty cycle, I_{rms} is the root-mean-square (RMS) value of the phase current [12]. The duty cycle D is determined by superimposing a third harmonic onto the reference voltage. It can be expressed in terms of the modulation index M as

$$D(\omega t) = \frac{1}{2} \left(1 + M \sin(\omega t) + \frac{1}{6} M \sin(3\omega t) \right). \tag{13}$$

Switching losses arise from the energy consumed during the turn-on and turn-off transitions of the transistors. These losses are typically characterized by the energy values E_{on} and E_{off} which are provided in the device datasheet. Let f_{sw} denote the switching frequency of the inverter. The average switching losses per semiconductor device are given by

$$P_{sw} = \frac{1}{2\pi} \int_0^{\pi} [E_{on}(\omega t) + E_{off}(\omega t)] f_{sw} d(\omega t). \tag{14}$$

Upon entering ASC mode, the high-side transistors remain continuously on. The total power losses in these transistors can be calculated as:

$$(i_a^2 + i_b^2 + i_c^2) R_{on} = K_{dq-abc} (i_d^2 + i_q^2) R_{on} \tag{15}$$

where $K_{dq\text{-}abc}$ is the scaling factor of d-q transformation. Equation (15) indicates that the total inverter losses depend on the stator dq-axis currents, which are independent of the initial rotor position. However, the losses in individual phases are proportional to the square of the phase current. As equation (10) shows, the phase currents vary with the initial rotor position, and therefore the transistors in different phases may experience different temperature rises depending on the rotor position at the moment ASC is triggered.

C. Thermal Model

Within the short timescale of ASC, the heat diffusion occurred in the transistor is limited due to the small thermal time constant of the transistor chip. Therefore, a accurate model describing the device's thermal characteristics is essential. Fig. 3 provides an overview of the thermal model. A typical SiC MOSFET module consists of multiple layers. The semiconductor layer is located at the top of the package and is directly bonded to a Direct-Copper-Bonded (DBC) substrate. The DBC layer provides both electrical isolation and high thermal conductivity between the semiconductor and the baseplate. At the bottom of the module, the baseplate connects the device to an external heat sink, facilitating the heat dissipation. The heat sink can be modeled as a thermal resistance connected to a reference temperature T_{amb}.

To model the thermal behavior of the device, either Foster or Cauer thermal networks can be used[13]. In this study, the Cauer model is adopted, as it more accurately represents the physical structure of the module and provides direct access to junction temperature calculations.

The thermal networks of the high-side and low-side modules in each phase are connected in parallel. It is assumed that modules from different phases are thermally isolated, meaning the temperature rise in one phase does not affect the others.

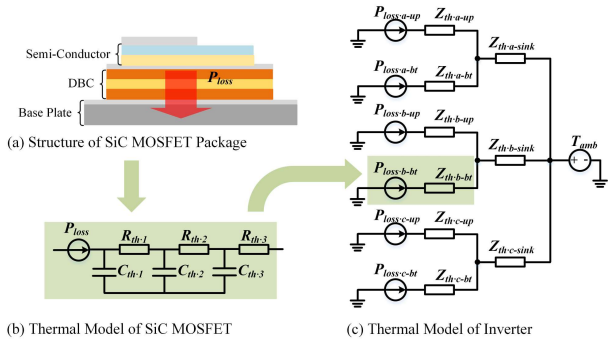


Fig. 3 Thermal model of three-phase SiC MOSFET inverter

III. Simulation of Drive System Under ASC Mode

A. Machine Model

In an electric machine, the dq-axis incremental inductances L_d and L_q are functions of the corresponding axis currents due to the magnetization property of the lamination used in the machine. To capture the current-dependent incremental inductances, a parametric sweep is performed using finite element method (FEM) analysis on the electromagnetic model of the machine.

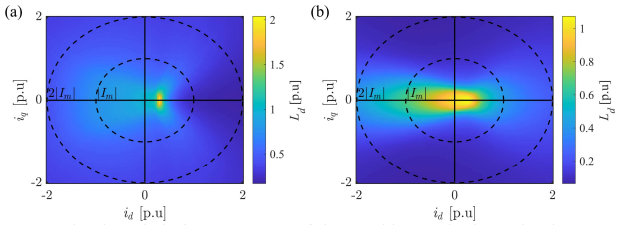


Fig. 4 The dq-axis inductance map of the machine under investigation. (a). d-axis inductance L_d. (b). q-axis inductance L_q.

Assuming the maximum steady-state current I_m is one p.u., lookup tables are generated to represent the inductance values over the dq-axis currents ranging from -2 p.u. to 2 p.u, as shown in Fig. 4. The dq-axis inductances are one p.u. when the stator current is zero.

The dq-axis flux linkages ψ_d and ψ_q are calculated as shown in Fig. 5. The dq-flux linkages are one p.u. when the stator current is zero. Assuming that the rotor flux linkage is aligned with the d axis, the rotor flux linkage ψ_m can be calculated as follows:

$$\psi_m = \psi_d - L_d i_d \tag{16}$$

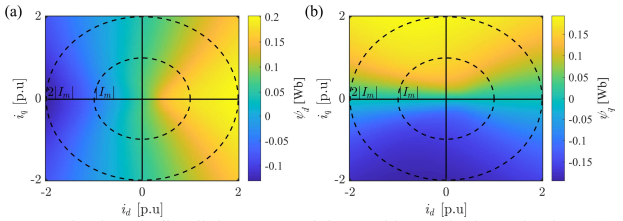


Fig. 5 The dq-axis flux linkage map of the machine under investigation. (a). d-axis flux linkage ψ_d. (b). q-axis inductance ψ_q.

With the inductance and flux linkage map of the machine, the reference currents of the machine under different operating points can be determined. The maximum torque per ampere (MTPA), the flux weakening and the maximum voltage per ampere (MTPV) currents of the machine are calculated. In this paper, the dq-current of the machine is controlled before activating the ASC. The MTPA strategy is used when the rotating speed is lower than the base speed, and the flux weakening strategy is used when the speed is higher. When the speed reaches three times of the base speed, MTPV strategy is used due to the limited voltage.

B. Investigation into Worst Initial Rotor Position

To evaluate the impact of rotor position on ASC current, simulations are conducted at a base speed operating point with rated torque. The rotor speed is assumed to be constant throughout the ASC event. The machine under investigation has a base mechanical speed of n_b=3000 RPM.

In this paper, assuming the base speed is one p.u., and the rated torque is one p.u. Once the machine reaches steady-state operation with the specified dq-current, ASC is triggered at different time instants with different initial rotor positions θ_0.

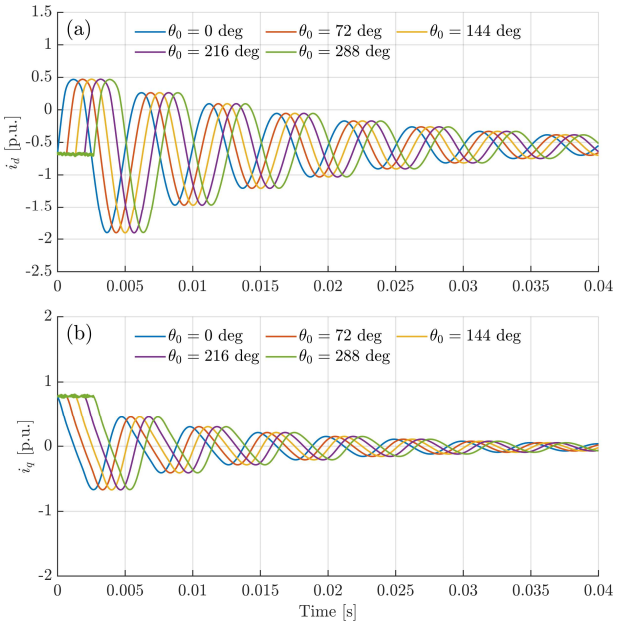


Fig. 6 The transient dq-axis currents with different initial rotor positions @ T_e^* = 1, ω^*=1. (a). d-axis current; (b). q-axis current.

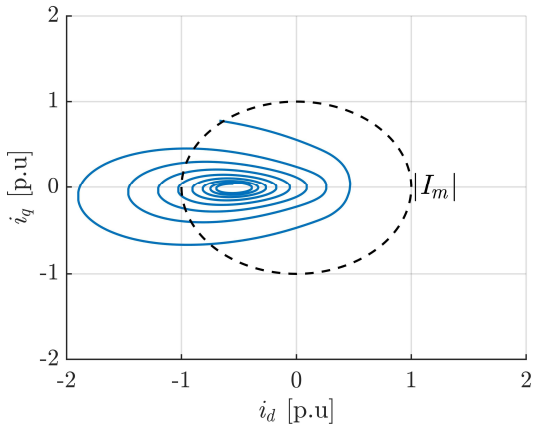


Fig. 7 The trajectory of stator current @ T_e^*= 1, ω^*=1.

Fig. 6 shows the d- and q-axis current responses for five different initial rotor positions: θ_0=0˚, 72˚, 144˚, 126˚, and 288˚. Regardless of the rotor position, the dq-axis currents exhibit similar transient behavior, confirming the analytical result from equation (9) that the dq-axis currents are independent of θ_0. After ASC is triggered, the currents begin to oscillate and decay exponentially, typically reaching steady state within 10 rotor cycles. The current trajectory, shown in Fig. 7, highlights the oscillations and the overshoot beyond the nominal current circle $|I_m|$. It can be observed from Fig. 7 that the current reaches a steady state with $i_q \approx 0$ and $i_d \approx \psi_m/L_d$. This result shows a good agreement with equation (9) with the stator resistance $R_s \approx 0$.

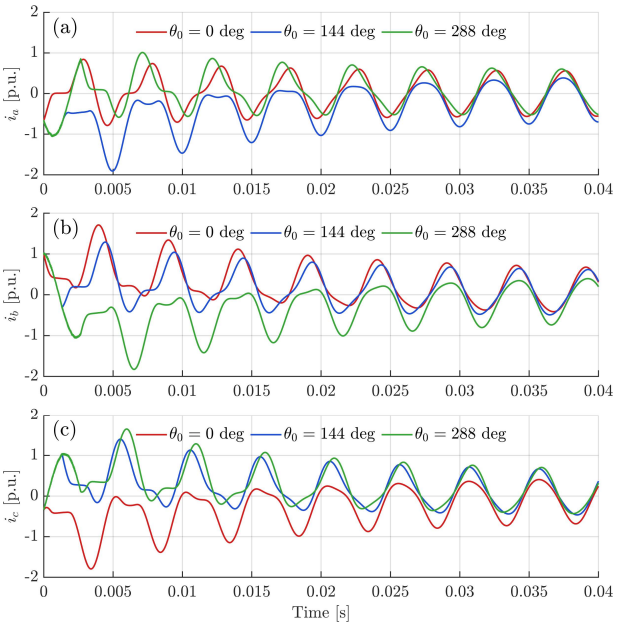


Fig. 8 The transient phase currents with different initial rotor positions (@ T_e^*= 1, ω^*=1). (a). Phase A current; (b). Phase B current; (c). Phase C current.

To further assess the influence of rotor position, phase currents are analyzed. Fig. 8 presents the phase current waveforms for three rotor positions θ_0 = 0˚, 144˚, 288˚. The peak current appears in different phases depending on the rotor position, leading to unequal losses and unbalanced temperature across the different phases of the inverter.

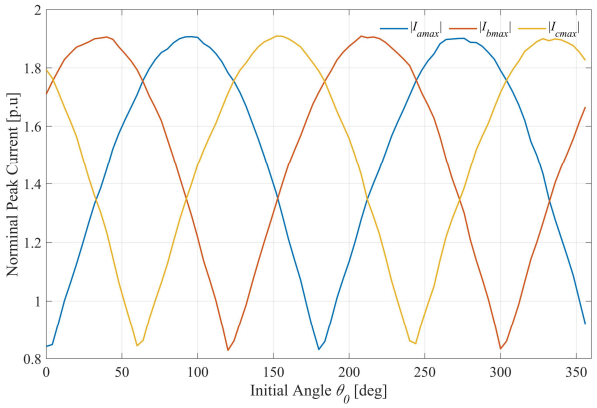


Fig. 9 The peak currents reached by phases at different initial rotor positions θ_0 @ T_e^*= 1, ω^*=1.

Fig. 9 summarizes the absolute peak current $|I_{(abc)max}|$ observed in each phase as a function of θ_0 when the machine operates with full torque and base speed (i.e. T_e^*= 1, ω^*=1). It is evident that the maximum current occurs in only one phase for a given θ_0, and this peak shifts between phases with 60˚ increment in the initial rotor position. Therefore, subsequent analysis focuses on phase A.

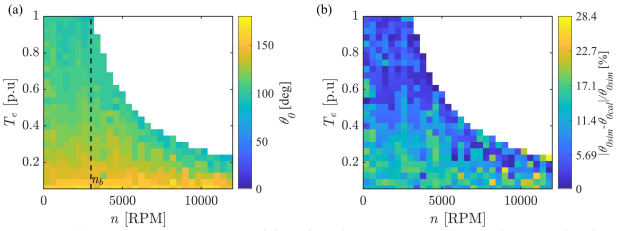


Fig. 10 The worst-case rotor position for phase A. (a). Simulation result; (b). The difference between simulation θ_{0sim} and theoretical calculations θ_{0cal} (in percentage).

The worst-case rotor position for phase A, defined as the position yielding the highest peak current, is investigated across various operating points. Fig. 10(a) shows the worst-case rotor position obtained from the simulation. The result indicates that the worst rotor position is primarily influenced by the machine torque, which is determined by the d- and q-axis currents, while the rotor speed has only a minor effect. The analytical worst-case rotor position from equation (11) is calculated and compared with the simulation results in Fig. 10(b). The difference between the two is likely caused by the time-varying dq-axis inductances used in the simulation, which are not captured in the analytical model.

C. Investigation into Junction Temperature of Transistor

Based on the simulation results from the previous subsection, the worst-case rotor positions for each operating point are selected to evaluate the highest junction temperature in phase A. In this simulation, the SiC power module CAB3R5M12DM4 is used to suit the maximum power of the machine. The thermal resistance of the heat sink is set to 0.06 K/W for water cooling with copper tube. The ambient temperature is set to $T_{amb} = 25\ ^{\circ}\mathrm{C}$.

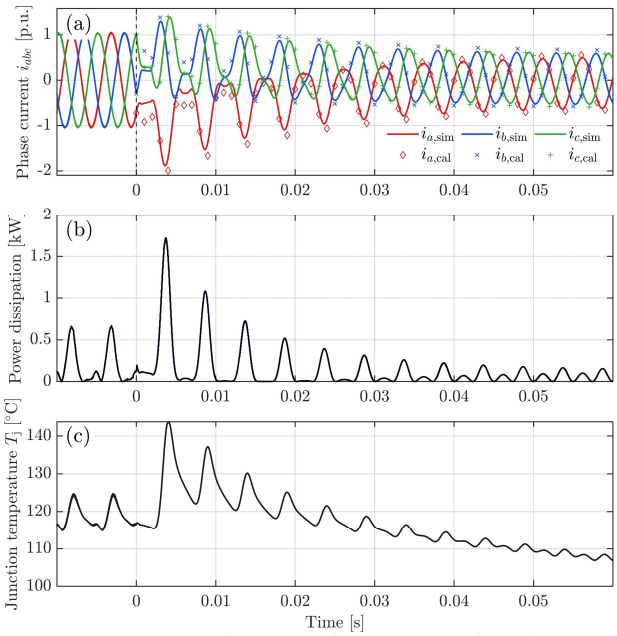


Fig. 11. Phase current from simulation and calculation; (b). Power dissipation on the phase A upper MOSFET; (c). The junction temperature of the MOSFET. @T_e^*= 1, ω^*=1, θ_0=96°.

Fig. 11 presents the phase current waveform (see Fig. 11(a)), the corresponding power dissipation in the transistor (see Fig. 11(b)), and the resulting junction temperature (see Fig. 11(c)). A comparison between theoretical calculations and simulation results for the phase current is also shown in Fig. 11 (a), demonstrating good agreement between simulation and theoretical calculation.

Following ASC activation, a surge in power dissipation is observed due to the rapid increase of current. This leads to a rapid increase in junction temperature T_j, due to the low thermal capacitance of the transistor. To assess the thermal impact across different operating conditions, five operating points with varying machine speeds and reference torques are simulated using the worst-case rotor position. The worst θ_0 for each case is obtained from Fig. 10.

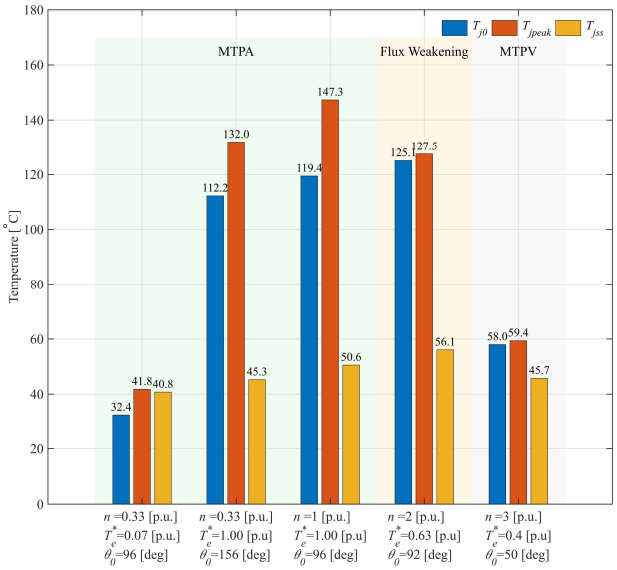


Fig. 12 Simulation result of the average junction temperature before ASC T_{j0}, the peak junction temperature during ASC T_{jpeak}, and the steady-state temperature after ASC T_{jss}, for different operating points of the machine.

Fig. 12 summarizes the junction temperature before ASC T_{j0}, the peak temperature during ASC T_{jpeak}, and the steady-state temperature after the transient T_{jss}. When the motor operates below the base speed, the MTPA control strategy is applied. In this region, the initial junction temperature T_{j0} is relatively high because rated torque requires a large stator current. When the speed exceeds the base speed, the machine enters the flux-weakening region, where the stator current remains high to compensate the increase of back-EMF at high speed and produce the specified torque, leading to a similarly high T_{j0}. As the speed increases further to approximately three times the base speed, the operating point change into the MTPV region, in which the phase current is limited by the DC-link voltage. Hence, the phase current is smaller and the T_{j0} decreases.

From the simulation results of the peak junction temperature T_{jpeak} after triggering ASC, the most critical condition occurs when the machine operates at base speed with rated torque, resulting in the highest temperature rise. The steady-state ASC temperature T_{jss} remains below the device's thermal limit due to the significantly reduced current in the steady-state ASC condition.

IV. Conclusion

ASC is a safe short-time operating mode for PMSM in automotive applications. However, the transient current during ASC can exceed the nominal current of the system, imposing significant thermal stress on the power inverter.

This paper investigates the thermal impact of surge currents on traction inverters during the ASC. A transient current model for PMSM under ASC mode is introduced, and the performance of a drive system with a three-phase inverter and a PMSM is analyzed. The worst initial rotor positions, which result in the highest peak phase current, are identified across the full operating range of the machine.

Subsequently, using the loss and thermal models of the inverter introduced in this paper, a case study in PLECS is conducted to evaluate junction temperature variations during ASC transient. Multiple operating points of the machine are examined to determine the conditions that lead to the highest

thermal stress. Results indicate that the most critical scenario occurs when ASC is triggered with machine operating at base speed and rated torque.

REFERENCES

[1] I. Husain *et al.*, "Electric Drive Technology Trends, Challenges, and Opportunities for Future Electric Vehicles," *Proc. IEEE*, vol. 109, no. 6, pp. 1039–1059, Jun. 2021, doi: 10.1109/JPROC.2020.3046112.

[2] S. Batchu, "Functional Safety in Inverter Hardware," presented at the International Mobility Conference, SAE International, Feb. 2016. doi: 10.4271/2016-28-0166.

[3] C. Gong, J. Liu, Z. Han, and H. Yu, "Analysis on uncontrolled generation in electrical vehicles and a battery protection method," in *2017 IEEE 3rd International Future Energy Electronics Conference and ECCE Asia (IFEEC 2017 - ECCE Asia)*, Jun. 2017, pp. 1606–1610. doi: 10.1109/IFEEC.2017.7992287.

[4] S. Chen, X. Hao, C. Gao, and Z. Jiang, "An Effective Nontransient Active Short-Circuit Method for PMSM in Electric Vehicles," *IEEE Trans. Ind. Electron.*, vol. 70, no. 4, pp. 3571–3580, Apr. 2023, doi: 10.1109/TIE.2022.3176315.

[5] A. Ruiz, A. Meseamanolis, L. Santolaria, M. Maleki, and A. Baschnagel, "Active Short Circuit Capability of HalfBridge Power Modules Towards EMobility Applications," in *PCIM Europe digital days 2021; International Exhibition and Conference for Power Electronics, Intelligent Motion, Renewable Energy and Energy Management*, May 2021, pp. 1–7. Accessed: Nov. 08, 2025. [Online]. Available: https://ieeexplore.ieee.org/document/9472249

[6] W. Q. Chu and Z. Q. Zhu, "Analytical modeling and investigation of transient response of PM machines with 3-phase short-circuit fault," in *2011 IEEE International Electric Machines & Drives Conference (IEMDC)*, May 2011, pp. 125–130. doi: 10.1109/IEMDC.2011.5994785.

[7] K. W. Klontz, T. J. E. Miller, M. I. McGilp, H. Karmaker, and P. Zhong, "Short-Circuit Analysis of Permanent-Magnet Generators," *IEEE Trans. Ind. Appl.*, vol. 47, no. 4, pp. 1670–1680, Jul. 2011, doi: 10.1109/TIA.2011.2154370.

[8] L. Fang, T. Sai, M. Kai, and L. Yan, "An Investigation of ASC Peak Current Suppression Method for Permanent Magnet Synchronous Motors," *Lect. Notes Electr. Eng.*, vol. 1016, pp. 688–695, 2023.

[9] K. Yao, H. Yano, H. Tadano, and N. Iwamuro, "Investigations of SiC MOSFET Short-Circuit Failure Mechanisms Using Electrical, Thermal, and Mechanical Stress Analyses," *IEEE Trans. Electron Devices*, vol. 67, no. 10, pp. 4328–4334, Oct. 2020, doi: 10.1109/TED.2020.3013192.

[10] X. Zhou, H. Su, Y. Wang, R. Yue, G. Dai, and J. Li, "Investigations on the Degradation of 1.2-kV 4H-SiC MOSFETs Under Repetitive Short-Circuit Tests," *IEEE Trans. Electron Devices*, vol. 63, no. 11, pp. 4346–4351, Nov. 2016, doi: 10.1109/TED.2016.2606882.

[11] K. Suzuki, K. Kashimura, H. Yano, and N. Iwamuro, "Unique short-circuit failure mechanisms in 1.2-kV SiC planar MOSFETs," *Appl. Phys. Express*, vol. 17, no. 12, p. 124002, Dec. 2024, doi: 10.35848/1882-0786/ad9980.

[12] A. Acquaviva, A. Rodionov, A. Kersten, T. Thiringer, and Y. Liu, "Analytical Conduction Loss Calculation of a MOSFET Three-Phase Inverter Accounting for the Reverse Conduction and the Blanking Time," *IEEE Trans. Ind. Electron.*, vol. 68, no. 8, pp. 6682–6691, Aug. 2021, doi: 10.1109/TIE.2020.3003586.

[13] A. S. Bahman, K. Ma, and F. Blaabjerg, "A Lumped Thermal Model Including Thermal Coupling and Thermal Boundary Conditions for High-Power IGBT Modules," *IEEE Trans. Power Electron.*, vol. 33, no. 3, pp. 2518–2530, Mar. 2018, doi: 10.1109/TPEL.2017.2694548.